Research Paper
J. Astron. Space Sci. 42(4), 97-118 (2025)
https://doi.org/10.5140/JASS.2025.42.4.97

JASS Journal of Astronomy and Space Sciences

Luminance Within Lunar Permanently Shadowed Regions

Robert Vernon Wagner[1,2†], **Mark Southwick Robinson**[1,2]
[1]School of Earth and Space Exploration, Arizona State University, Tempe, AZ 85287, USA
[2]Intuitive Machines, Phoenix, AZ 85042, USA

Exploration of the lunar poles is accelerating as multiple missions target these regions, with growing interest in studying the environment within permanently shadowed regions (PSRs)—areas at the poles that never receive direct sunlight. To prepare for these exploration activities within PSRs, we determined radiance levels in PSRs of various sizes and derived a conversion factor from ShadowCam radiance units to luminance, which is more suitable for evaluating human factors, as luminance accounts for the wavelength range to which humans are sensitive. Notably, during lunar summer, many PSRs reach luminance levels comparable to those of well-lit buildings for several Earth days each month, while peak winter lighting is typically up to six times dimmer, except in regions where regional shadows predominate and further decrease illumination. As a result, we do not expect artificial light to be needed for missions visiting PSRs during the summer peak lighting period, except for close inspection of samples. In contrast, in winter, diminished ambient lighting may require supplemental illumination for many tasks.

Keywords: Korea Pathfinder Lunar Orbiter (KPLO), Danuri, ShadowCam, Artemis, permanently shadowed region, secondary illumination

1. INTRODUCTION AND BACKGROUND

The lunar south polar region, and in particular the permanently shadowed regions (PSRs) therein, is hypothesized to harbor significant volumes of frozen volatiles (Watson et al. 1961; Arnold 1979; Lawrence 2016; Brown et al. 2022). Missions from a range of countries are in development to explore this region in search of volatiles, including VIPER, CP-22/IM-4, Chang'e 7, Chandrayaan-5/LUPEX, and Luna 27 missions, as well as the crewed Artemis 3 mission (Smith et al. 2020; Jia et al. 2023; Djachkova et al. 2022; Schonfeld 2024; Narendranath et al. 2025). With many of these missions intending to operate in or near PSRs, a key question is how much natural light will be available for navigation and geologic investigations within polar shadows.

Artemis 3 astronauts will not be the first to work in shadow on the Moon: on all of the Apollo missions, the Lunar Module ladder was in the shadow of the module, and on Apollo 16, the astronauts sampled from a permanent shadow, an overhang on the pole-facing side of the ~3 m high Shadow Rock (Station 13). While the astronauts typically mentioned that they had to pause to let their eyes adjust (and to raise the gold Sun shield on their helmets) after stepping into shadow, they also mentioned in multiple technical debriefings that they had no issues seeing in shadows after those adjustments (NASA 1969b, d, 1971c, 1972b). However, lighting at the poles is at a lower angle than on any Apollo traverse; the closest lighting humans have experienced on the Moon is the landing of Apollo 12, with an incidence angle (angle between the Sun vector and the zenith) of ~85°. Additionally, the most common shadow the astronauts worked in was the shadow of the Lunar Module, which, unlike shadows in craters, did not have a nearby raised sunlit surface (e.g., a crater wall) to provide significant illumination to the ground within it. Thus, further analysis of the polar lighting conditions is warranted to determine how the polar environment influences visibility within shadows.

Previous studies have modeled secondary irradiance

Received 09 AUG 2025 **Revised** 07 OCT 2025 **Accepted** 08 OCT 2025

†**Corresponding Author**
Tel: +1-281-520-3703, E-mail: rwagner@intuitivemachines.com
ORCID: https://orcid.org/0000-0001-5999-0721

https://janss.kr pISSN: 2093-5587 eISSN: 2093-1409

(light reflected into a shadow) in PSRs, focusing mainly on overall energy to determine surface ice stability, and calibrated their models to orbital data across the visible and thermal infrared ranges (Mazarico et al. 2011; Hayne et al. 2021; Mahanti et al. 2024). Mahanti et al. (2022, 2023) modeled secondary illumination specifically of visible light in order to better interpret ShadowCam images, although absolute calibration to ShadowCam radiance values is ongoing. Other studies have focused on human factors of operating in grazing sunlight near the lunar poles, but they have either left secondary illumination for future work (Null et al. 2023) or used non-physical (but computable in real time) reflected light models without explicit ties to empirical data or physics-based modeling (Litaker et al. 2025). Here, we use the ShadowCam instrument on the Korea Pathfinder Lunar Orbiter (KPLO), which is optimized to image inside PSRs, as a light meter to directly measure surface brightness under indirect (secondary) illumination. Calibrated ShadowCam observations provide radiance (W/m^2/sr/μm), with a strong response in the near infrared beyond the range of human vision. To account for the relatively narrow range of wavelengths that the human vision system is sensitive to, we developed a method to use the predicted spectra of light in lunar shadows to converted ShadowCam radiance measures to luminance (cd/m^2). Luminance (with units based on the SI lumen) uses the relative perceived brightness of different wavelengths and is commonly used in lighting specifications and photography.

We found that PSRs often have illumination levels comparable to comfortable indoor lighting levels. In summer, all but the very darkest PSRs can reach levels found in lit buildings and are bright enough for a human to navigate comfortably without artificial lighting, though in some cases additional light may be desired for inspecting geologic samples.

1.1 Terminology

In this work, we use four closely linked and similar sounding terms related to light levels within a scene: Radiance, irradiance, luminance, and illuminance. Radiance is the total electromagnetic radiation emitted/reflected by a surface, while irradiance is the electromagnetic radiation incident upon a surface. Both are measures of energy, with units based on watts and no inherent connection to a particular wavelength. Luminance is the intensity of light emitted or reflected from a surface, while illuminance is the intensity of light incident upon a surface, and both are measured in terms of wavelengths humans can sense with units derived from the SI base unit for luminous intensity, the candela (cd).

For lighting geometry, we use primary, secondary, and tertiary to indicate how many times sunlight is reflected before reaching the surface of interest. Primary illumination is light coming directly from the Sun. Secondary illumination is when light reflects from a sunlit surface and hits a surface inside a shadow. In some places, local terrain can block this secondary light, casting a “secondary shadow” or making the surface “doubly shadowed”, and the terrain in that shadow is only lit by tertiary illumination, sunlight that has first been reflected from two other surfaces. Further reflections do occur, but the resulting illumination levels are too low to detect in ShadowCam observations.

1.2 ShadowCam

The Korea Pathfinder Lunar Orbiter (KPLO, also known as Danuri) carries the NASA ShadowCam instrument, designed to image details of morphology and albedo in shadowed areas with pixel scales better than two meters (Robinson et al. 2023). ShadowCam images enable direct measurements of illumination levels inside shadows, both permanent and temporary. ShadowCam is based on the earlier Lunar Reconnaissance Orbiter Narrow Angle Cameras (LROC NACs; Robinson et al. 2010), with nearly identical optics and similar electronics, but with improvements to baffling and optics margins to reject stray light, and a different sensor technology. Instead of the NACs’ single-line line scan sensor, ShadowCam uses a time delay integration (TDI) sensor, and is roughly 200 times more sensitive than the NACs (Humm et al. 2023).

TDI sensors work by building up signal as successive lines pass over the target. In effect, each “stage” (line) of a TDI sensor is an additional single-line line scan camera placed in sequence: the electrical charge from each line is passed on to the next one at the same rate as the lines scan across the surface. This rate, and thus the per-line exposure time, is determined when planning an observation based on the orbital speed and ground distance, and exposure time cannot be adjusted based on expected surface brightness without introducing blurring. By accumulating the charge over multiple stages, the sensor can get an effective exposure time equal to the per-line exposure time multiplied by the number of stages. This allows sharp images with effective exposure times that would produce dozens of pixels of smear in a normal line-scan camera.

The sensor used in ShadowCam always reads out 128 TDI stages, so a key decision during development was the selection of how many stages would be used in the flight instrument; the remaining lines on the detector would be physically masked out. This decision was based on LROC NAC long exposure PSR radiance measurements. The final decision was to mask ShadowCam down to 32 stages in order to avoid detector saturation for terrain in PSRs while obtaining signal-to-noise ratios (SNRs) above 100 for as much PSR terrain as possible under optimal lighting (Humm et al. 2023). As predicted, ShadowCam only saturates when imaging sunlit terrain and the very brightest surfaces in the brightest polar shadows, and has imaged approximately half of all permanently shadowed lunar terrain at ≥100 SNR (~0.12 W/m^2/sr/μm) at least once.

ShadowCam is a panchromatic instrument, sensitive to wavelengths from ~400–800 nm. The uncertainty in the absolute radiometric calibration of ShadowCam is 6% (Humm et al. 2023), meaning that our luminance values could have a systematic bias of up to ± 6% due to the camera calibration.

ShadowCam began orbital imaging in January 2023 and has acquired images covering the full range of seasonal lighting variation in most kilometer-scale PSRs. Each ShadowCam image is 3,072 pixels wide by up to ~85,000 pixels long, with pixel sizes typically ranging from 1.6 to 2.0 m.

1.3 Luminance

Because human vision operates in a narrow range of frequencies and is dependent on the vagaries of biologic systems, the purely physics-based units of radiance are not suitable for describing perceived light levels and are inconvenient for predicting optimal exposure settings for visible-light cameras. For these purposes we turn to luminance, which is a measure of the brightness of a surface within the human vision range. Luminance is measured in units of candela per square meter (cd/m^2), which are also known as “nits” when discussing the brightness of televisions and computer monitors.

The SI base unit for luminous intensity, the lumen, is defined specifically for monochromatic light at 540 × 10^{12} Hz (555 nm wavelength), approximately the peak responsivity of the human eye under bright light. To determine luminance outside of that wavelength, we need to use a luminous efficiency function, which measures the perceived brightnesses of equal radiances of other wavelengths relative to 555 nm. The standard luminous efficiency functions are produced by the International Commission on Illumination (CIE) and vary depending on the viewer’s level of dark-adaptation and what area of the retina is observing the target (ISO 2023). For center-of-field-of-view work at high light levels (e.g., viewing details under normal indoor lighting and brighter), the photopic luminous efficiency function $V(\lambda)$ is used, and this is the recommended function for comparing light levels across all luminance levels (ISO 2023).

At lower luminance levels (below 5 cd/m^2), human vision transitions from photopic, which fully utilizes the color-detecting cones in our eyes, to mesopic, a mixed mode using both cones and rods with partial color vision and reduced detail, but higher overall sensitivity (and also a blue-ward shift of the sensitivity peak). Below 0.005 cd/m^2 is scotopic vision, purely rod-based with no color, poor detail resolution, and very high sensitivity. These transitions involve changes in chemistry in the retina and are not instantaneous, and they depend on not being exposed to photopic-level light sources for several seconds to minutes (“dark-adaptation”), depending on how dark the scene is (Null et al. 2023). While we expect astronauts to primarily operate with photopic vision, due to the presence of visible sunlit terrain with luminance levels likely above 300 cd/m^2 even when they are within shadows, they will be able to quickly partially dark-adapt by blocking out any sunlit surfaces or focusing on shadows, allowing their pupils to dilate and increasing their overall sensitivity to light.

We use the photopic luminous efficiency function $V(\lambda)$ for all calculations in this paper for three reasons: First, consistent conversion across all radiance levels simplifies comparisons and allows easy evaluation of non-human systems, such as commercial cameras. Second, we expect astronauts in PSRs to typically be operate in or near the photopic vision mode. This is because the bright sunlit terrain on the horizon (the source of the secondary light) will frequently be in their field of view. Third, even if astronauts adapt into the mesopic range, most PSRs have overall light levels in the upper part of that range. The human vision response there is more similar to the photopic curve than to the scotopic curve (IOS 2023).

Converting radiance to luminance requires that radiance is in spectral radiance form: radiance quantified at each wavelength over the 380 to 830 nm range of $V(\lambda)$. Given a spectral radiance curve $R(\lambda)$ of a surface in W/m^2/sr, the following equation gives the luminance of that surface in (photopic) cd/m^2 (ISO 2023):

$$luminance = \int_{380\text{ nm}}^{830\text{ nm}} R(\lambda) \times V(\lambda)\, d\lambda \times 683 \frac{\text{lm}}{\text{W}} \tag{1}$$

Our methodology for deriving $R(\lambda)$ and producing a conversion factor from radiance to luminance for ShadowCam images is given in Section 2.4.

1.4 Photographic Exposure Value

A convenient derived value from the luminance of a scene is exposure value (EV), a Log$_2$-scale measure used by photographers when determining optimal camera settings for a scene. An increase of 1 EV is a doubling of the scene luminance, allowing easy comparisons across the extremely wide sensitivity range of human vision. For ISO 100 film or equivalent digital sensor gain and a light meter calibration constant of 12.5, $EV = Log_2(L \times 100/12.5)$, where L is the scene luminance in cd/m^2 (ISO 1994). This is the conversion we use in this paper, though the standard allows calibration constants between 10.6 and 13.4, and actual cameras can of course be capable of sensitivities other than ISO 100 equivalent. Table 1 gives a list of EV and cd/m^2 levels with corresponding terrestrial and lunar scenes and other relevant notes.

Based on informal testing at various lighting levels (Section 3.3), we have marked two lighting levels relevant to astronauts on all our graphs: For ambient lighting levels that illuminate the surface to ~4 EV or higher, we do not expect astronauts to need artificial light except possibly for close examination of samples; below ~2 EV, we expect them to need artificial light for any geologic investigations, and possibly for traversing.

2. DATA AND METHODS

We collected radiance values for two classes of PSR: “large” and “small”, based on the minimum dimension of the permanent shadow, with the size thresholds chosen based on the processing methods needed for each. Our large PSRs are 8 km diameter and larger, while our small PSRs are < 500 m diameter. These two classes require significantly different processing. Large PSRs used an automated data collection method, while small PSRs required much more manual data collection and additional artifact correction.

In all cases, the source data were ShadowCam nadir-pointing images, calibrated to radiance units. Due to photometric effects, images with off-nadir viewing angles would have given a significantly higher or lower apparent surface radiance from identically lit nadir-looking images (Hapke 1981), and in some cases could have been contaminated by stray light artifacts from direct sunlight entering the ShadowCam baffle (Humm et al. 2023).

2.1 Data preparation: Large Permanently Shadowed Regions

We collected radiance statistics for 28 sites in large PSRs (≥ 8 km; Table 2), using an automated data-collection process to gather radiance statistics across a region up to ~8 × 8 km within each PSR. We first manually selected a

Table 1. Luminance levels of typical scenes in EV (for ISO 100 film) and cd/m^2

EV	cd/m^2	Examples[1)]
17	16,384	Snow field at noon[b]
16	8,192	Looking down onto the lunar surface at noon on the equator[a]
15	4,096	Noon on a clear day, typical nearby scene[b]
14	2,048	Planned luminance for Apollo down-Sun photography[c]
13	1,024	Planned luminance for Apollo cross-Sun photography[c]
12	512	Mean sunlit lunar surface near poles[a]
11	256	Sky at sunset[a,b], backlit scene moments before sunset on a clear day[a,b]
10	128	Late afternoon shadows[a]
9	64	Nighttime sporting events[b], typical ShadowCam saturation level[d]
8	32	Well-lit windowless office[a,e], open shade at sunset[a,b], brightest PSRs[a]
7	16	Minimum recommended lighting for office spaces[e]
6	8	Peak brightness of Shackleton crater in summer[a], ShadowCam signal-to-noise ratio 100 level[d], upper end of mesopic vision[f]
5	4	Minimum recommended lighting for corridors and stairways[e]
4	2	Well-lit roads at night[g]
3	1	Peak brightness of Shackleton crater in winter[a]
2	0.5	Peak summer brightness of darkest PSRs (Amundsen)[a]
1	0.25	Peak lunar luminance under Earthshine[h]
0	0.125	Beginning of nautical twilight[a]
–1	0.0625	Approximate ShadowCam lower detection limit[d]
–2	~0.0313	
–3	~0.0156	Outdoor nearby scene lit by a full Moon[b], lower end of mesopic vision[f]

[1)] References: [a] This work. [b] ANSI (1973). [c] NASA (1971a, b). [d] Humm et al. (2023). [e] ANSI (1993). [f] Kunkel & Reinhard (2010). [g] Alferdinck (2006). [h] Wagner et al. (2023).
EV, exposure value; PSRs, permanently shadowed regions.

Table 2. Large PSRs evaluated in this work

Name	Latitude[1]	Longitude[1]	Crater diameter (km)	PSR Size (km)	Depth/Diameter
Amundsen	–83.679	91.434	103	31 × 23	0.035
Brill	–88.325	266.245	17	21 × 17	0.090
Cabeus (1)	–84.479	315.814	101	28 × 19	0.040
Cabeus (2)	–84.590	312.000	101	28 × 19	0.040
Cabeus B	–81.766	305.738	60	24 × 22	0.062
Faustini	–87.039	84.691	42	30 × 29	0.066
Fibiger	86.119	37.504	21	13 × 12	0.057
Haworth	–87.558	358.227	51	36 × 35	0.061
Hermite	84.805	250.165	109	22 × 21	0.032
Hermite A	87.973	310.700	20	17 × 16	0.145
Hinshelwood	89.381	311.760	13	9 × 9	0.084
Idelson L	–83.971	119.469	28	21 × 20	0.096
Lovelace	81.678	250.658	57	24 × 20	0.069
Lovelace E	81.972	263.224	22	14 × 13	0.125
Nansen F	84.394	61.189	62	23 × 19	0.038
Roz. K	81.998	213.107	43	25 × 18	0.084
Roz. U	84.640	153.572	44	24 × 23	0.069
Scott E	–81.008	35.859	29	16 × 14	0.096
Shackleton	–89.680	127.260	21	17 × 17	0.187
Shoemaker	–88.225	46.372	52	38 × 35	0.063
Slater	–88.153	113.408	25	21 × 14	0.044
Spudis	–89.550	278.030	13	8 × 8	0.102
Stose	–86.413	31.907	17	13 × 12	0.134
Sverdrup	–88.213	215.301	33	35 × 23	0.055
Sylvester	82.222	277.000	59	25 × 18	0.060
Sylvester N	82.417	291.146	20	14 × 14	0.190
Weichert J	–85.213	183.506	35	23 × 20	0.090
Whipple	89.095	121.046	15	12 × 9	0.184

[1] Latitude and longitude are for target point, not center of crater.
PSR, permanently shadowed region; Roz, Rozhdestvenskiy.

target point near the center of the PSR that did not have topographic relief that might cause significant secondary shadowing within ~1 km of the target point. We then ran a process that extracted a 1,200 × 1,200 m patch centered on the target point from each ShadowCam image that covered that area and recorded the median radiance of that patch, along with the time of day and season (sub-solar latitude). Images with median radiances below 0.0004 W/m^2/sr/μm (~ –2 EV) were recorded as off-scale low, as such values are typically below the noise floor of the ShadowCam detector for nadir imaging in the 100 km primary mission orbit. We excluded all images with <95% coverage of the 1,200 × 1,200 m area.

We then repeated that data collection process for 80 additional points surrounding the target point in a 9 × 9 grid, with 900 m spacing between points, aligned to the latitude-longitude grid, to determine regional variability (Fig. 1 inset). Any patch containing terrain that was not in a PSR was excluded to avoid any potential for contamination from direct sunlight. Results are shown in Section 3.1. While our smallest "large" PSR had a minimum dimension of 8 km, this fully automated data collection method could be extended down to ~2 km diameter PSRs, although at that point the target point will be the only remaining patch.

2.2 Data preparation: Small Permanently Shadowed Regions

ShadowCam was designed to significantly reduce internal stray light (signal due to internal scattering within the camera optics) relative to the LROC NAC design (Humm et al. 2023). The design reduces stray light from outside the field of view by up to 100× compared to the LROC NAC (~20–100× for sources within 9.5° of the field of view, up to 2.5× for sources outside 13°). The net out-of-field stray light signal is on the order of 0.2% of the mean radiance of all terrain within ~2° outside the camera's field of view (~3.5 km surrounding the image), weighted strongly towards the closest terrain, with only negligible contributions from terrain beyond that distance (Humm et al. 2023). However, small patches of directly-illuminated terrain within the field of view also have localized "halos" of stray light (Fig. 2(a)), primarily in the along-track direction, which are on the order of 0.2%–0.7% of the radiance of the directly-illuminated terrain (Humm et al. 2023). Outside of this halo,

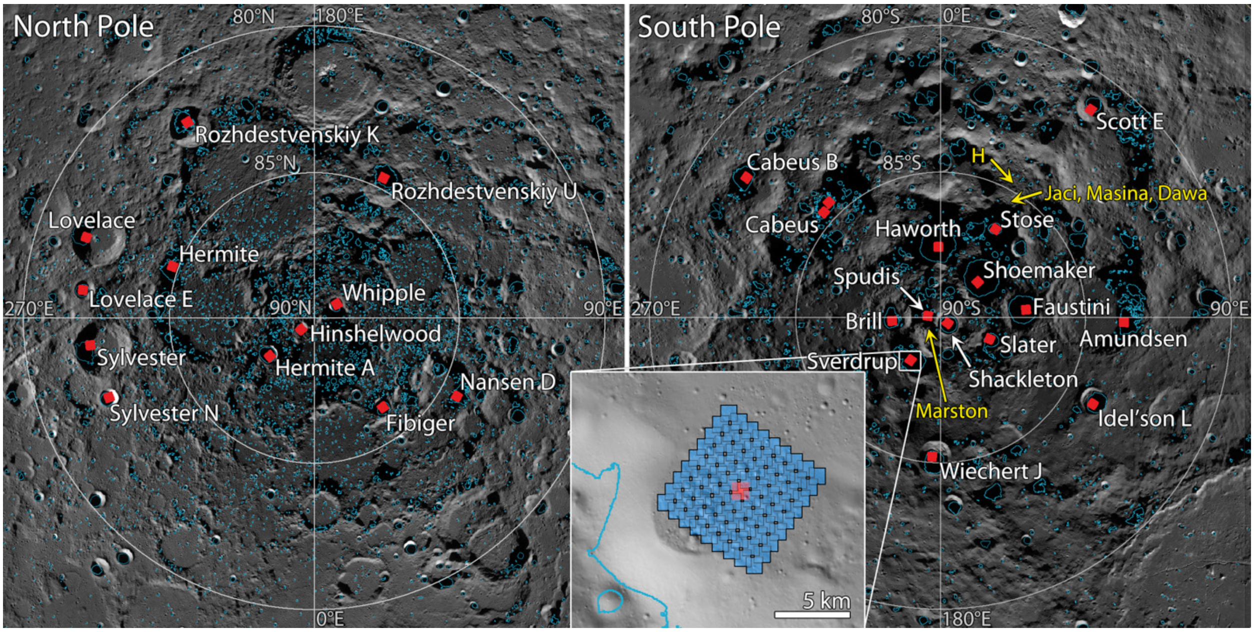

Fig. 1. Locations of the PSRs measured in this paper. Red squares with white labels in the main panels mark the area measured for large PSRs, yellow text denotes small PSRs listed in Section 2.2, and blue outlines mark boundaries of all PSRs at each pole. Inset: Locations of the target point (red) and surrounding points (blue) for Sverdrup PSR overlain on shaded relief of terrain model. PSR, permanently shadowed region.

the telescope design reduces in-field stray light to negligible levels. For shadowed regions within ~150 pixels of directly illuminated terrain (~260 m from the nominal 100 km altitude orbit), that < 1% stray light artifact is often stronger than the signal from the underlying terrain, though it falls off rapidly from ~150 to ~200 px from the sunlit terrain. This illustrates both the extreme radiance contrasts in these images and the difficulty in accurately determining the true surface radiance in regions near directly illuminated terrain. For PSRs with a shadowed area < 600 m wide, the whole shadow can be significantly contaminated by stray light for typical ShadowCam pixel scales of 1.6–2.0 m.

We do not have a numerical model to correct the stray light contribution. A proper correction would require knowing the actual radiance from each directly-illuminated pixel; ShadowCam only records that the detector is saturated, which typically occurs around 0.75 W/m^2/sr/μm, while illuminated polar terrain is typically ~5–20 W/m^2/sr/μm based on LROC NAC observations. However, for the small PSRs in this study, we coarsely bound the stray light component for that individual shadow. As an upper bound, the stray light contribution cannot be higher than the lowest recorded value in the area it contaminates (Humm et al. 2023). As the stray light signal is not constant, the lowest radiance value pixel in a shadow may not lie within the region of highest stray light signal, particularly in low-Sun cases where the shadows are wider than ~600 m (in such cases, a better stray light correction might be to select the darkest pixel within 300 m of saturated terrain). However, in the most severe stray light conditions, with shadows smaller than ~300 m diameter and sunlit areas on all sides at least as large as the shadow (both of which are usually true at the peak lighting time for the small PSRs in this study), the stray light signal should be roughly constant across the shadow. Thus, in the brightest cases (e.g., Fig. 2(b)), our stray light bounds should be equal to the true stray light (or higher, if there is any detectable tertiary lighting), and thus our adjusted luminance values should be less than or equal to the true luminance (that is, an astronaut may find that the crater is brighter than we predict, but probably not darker). In less-optimally-lit conditions (shadows > 300 m or large nearby shadows, more common towards dusk or dawn or in winter), our luminance estimates could be either higher or lower than the true values (see examples in Section 3.2.1).

We also approximate stray light intensity from nearby similarly-sized shadows, equally surrounded by illuminated terrain, but without identifiable terrain features (indicating a lack of measurable secondary light). This estimate usually requires alcoves on the down-Sun side of a ridge, with no Sun-facing slope providing secondary illumination. This method generally produces an estimated stray light component that is lower by a factor of two than the lowest-radiance-pixel method (Fig. 2(b)).

We obtained radiance values from nadir-looking images

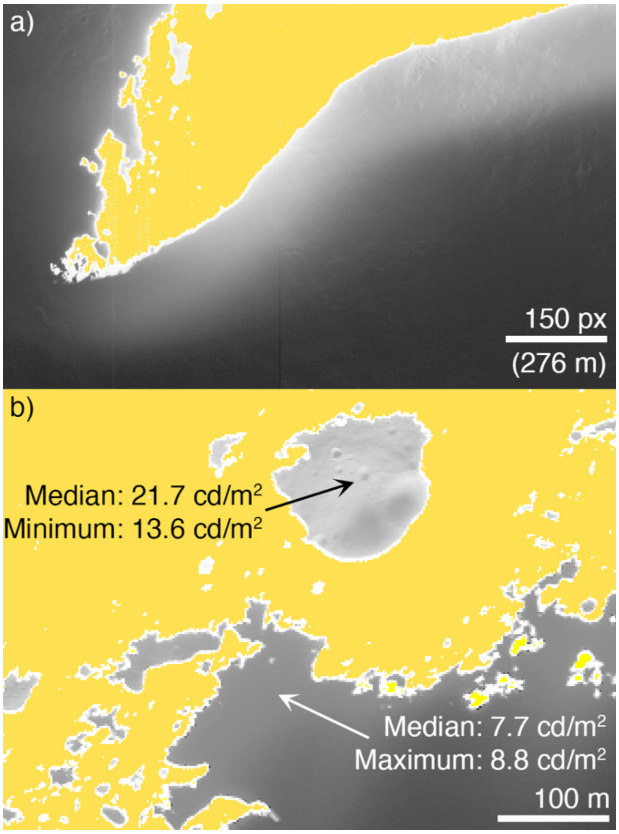

Fig. 2. ShadowCam stray light halos. (a) In-field stray light in M039293869S; yellow indicates saturation (direct sunlight). Stray light signal is ~1.5× the radiance of the underlying terrain, but < 0.5% of the radiance of the saturated area (based on similarly-lit LROC NAC images), and extends ~150 px from saturated area in the unprojected image. (b) Stray light inside Marston crater. Minimum value within crater is higher than median value in a similarly-sized shadow with no identifiable terrain inside. Both panels have gamma stretches applied to show detail across the dynamic range.

calibrated to radiance and map-projected at 2 m/px. For each image, we first masked all pixels within 18 m (9 pixels) horizontally or vertically from any saturated terrain, as those pixels are frequently contaminated with additional detector artifacts (Humm et al. 2023) and may also contain some non-saturated terrain directly illuminated by a sliver of the solar disk. We then manually selected a rectangular box containing all remaining shadowed pixels within the crater of interest and as little shadowed terrain outside as possible, and recorded the median and minimum radiance in that box. The shadowed area measured varied based on lighting; we did not restrict our analysis to just the permanently shadowed part of each crater. Additionally, since the data collection process required inspecting every image manually, we marked all images where > 50% of the shadow area was filled with featureless noise as off-scale low, as that indicates that the only detected signal was from stray light. Results are shown in Section 3.2.

In this work, we investigate five small-scale PSRs (Table 3 and Fig. 1). Marston (unofficial name) is near the crest of the Shackleton-de Gerlache ridge, on the Earth-facing side (Fig. 2(b)). H crater (unofficial name) is very similar in size to Marston, but ~5° further from the pole, and is ~900 m north of the Intuitive Machines IM-2 landing site on Mons Mouton. Jaci, Masina, and Dawa are three craters within the ~4 km wide intended destination area for the VIPER mission, also located on Mons Mouton (Beyer et al. 2025); all three are more degraded than Marston and H craters. Jaci is the largest and steepest-walled of the three, with frequent 20° slopes, while Masina is smaller and more degraded, with typical slopes around 10°, but still has a clear crater morphology. Dawa is an irregular depression defined primarily by the rims of Jaci and Masina. It has much less prominent equator-facing walls than the other two (slopes on the equator-facing walls are typically < 5°, overall slopes are < 10°).

2.3 Data Binning

We compare our measurements to two measures of local lighting, time of day and season, both derived from the location of the sub-solar point (the intersection of the Sun-Moon vector with the lunar surface) relative to the location of interest.

Local time of day is a 24-unit measure of local lighting direction, calculated as:

$$\text{local time of day} = \frac{\left[\left(\text{local longitude} - \text{sub-solar longitude}\right) + 360\right]\%360}{360^\circ} \times 24 + 12 \qquad (2)$$

where "a%b" gives the remainder of a/b. Sunrise is nominally 6.0, sunset is nominally 18.0, and 12.0 marks the Sun at its highest point in the sky (noon), although actual sunrise and sunset times vary considerably near the poles depending on regional topography and can occur multiple

Table 3. Locations of the small PSRs in this study

Name	Latitude	Longitude	Crater diameter (m)	PSR dimensions (m)
Marston[1)]	-89.475	223.192	220	100 × 80
H[1)]	-84.761	29.166	200	100 × 70
Jaci	-85.414	31.100	1.8	580 × 350
Masina	-85.410	32.193	1.4	500 × 200
Dawa	-85.450	31.616	650	250 × 200

[1)] Unofficial name.
PSRs, permanently shadowed regions.

times in a single lunation. Note that since longitude increments rapidly with distance at the pole, we always use the center of the site of interest as the local longitude to compare the solar longitude to (that is, we use the longitude of the central target point as the local longitude for all 81 patches in the large PSRs), so that a single Sun position gives the same time of day for all sample points in the PSR.

We assign images to one of three season groups based on sub-solar latitude, after reversing the sign of sub-solar latitudes for south polar sites so that positive always means the sub-solar point is on the side of the equator closest to the site of interest. Summer: > 1.0; Equinox: 0.5 to –0.5; Winter: < –1.0 (sub-solar latitudes on the Moon span a range of up to ~ ± 1.6 over the course of a year). We do not show the data for sub-solar latitudes between those seasons (sub-solar latitudes ± 0.5–1.0), as they typically overlap the adjacent seasons enough to hinder readability, but differ enough to significantly change average radiance if binned with either group.

2.4 Luminance Conversion

As described in Section 1.3, we use luminance units (cd/m^2) to express what a human would experience in a shadow, but ShadowCam is calibrated to radiance (W/m^2/sr/μm from approximately 400 to 800 nm; Humm et al. 2023). Since ShadowCam is sensitive over a broader wavelength range than the human eye [as measured by the luminous efficiency function $V(\lambda)$, Fig. 3], we cannot use ShadowCam as a direct proxy for a human eye, and instead need to derive a conversion factor from ShadowCam radiance values to luminance. Because ShadowCam is a single-band panchromatic instrument, we calculate the spectrum of the light it detects from first principles by combining the source (solar) spectrum with the reflectance spectrum of each surface (Fig. 4). We use the solar spectrum [denoted by $S(\lambda)$; ASTM 2019], the reflectance of the illuminated lunar highlands surface [$M(\lambda)$; from Robotic Lunar Observatory Apollo 16 reflectance (Ohtake et al. 2013) extended to 360 nm with LROC WAC data (Mahanti et al. 2016)], the reflectance of the indirectly-illuminated lunar surface [$M(\lambda)$ again], the sensitivity spectrum for ShadowCam [$C(\lambda)$; Humm et al. 2023], and the sensitivity spectrum for the LROC NACs [$N(\lambda)$; Humm et al. 2015]. See Fig. 3.

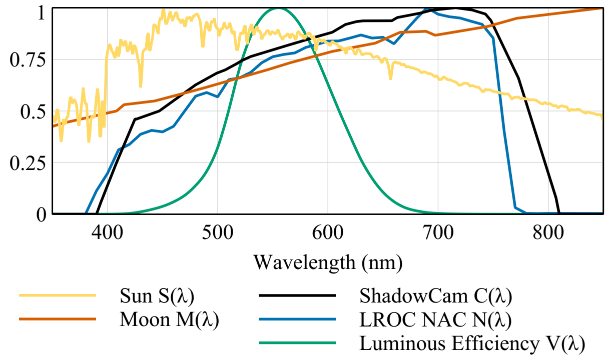

Fig. 3. Spectra and response curves used in this analysis: Sunlight $S(\lambda)$, lunar highlands reflectance $M(\lambda)$, ShadowCam responsivity $C(\lambda)$, LROC NAC mean responsivity $N(\lambda)$, and luminous efficiency function $V(\lambda)$. All spectra have been scaled to the range 0–1. LROC NACs, Lunar Reconnaissance Orbiter Narrow Angle Cameras.

All luminance calculations were performed on spectra sampled at 1 nm intervals; where the source spectra were defined at larger intervals, we sampled a piecewise linear interpolation between the points that were defined. Spectra $M(\lambda)$ and $N(\lambda)$ were extracted from figures in their respective source papers using WebPlotDigitizer (Rohatgi 2024); all others were provided in tabular format. All source and interpolated spectra used are available in the Supplementary data.

To calculate luminance, we first find the spectral power distribution reflected from the surface towards ShadowCam that produces a given ShadowCam radiance value, here

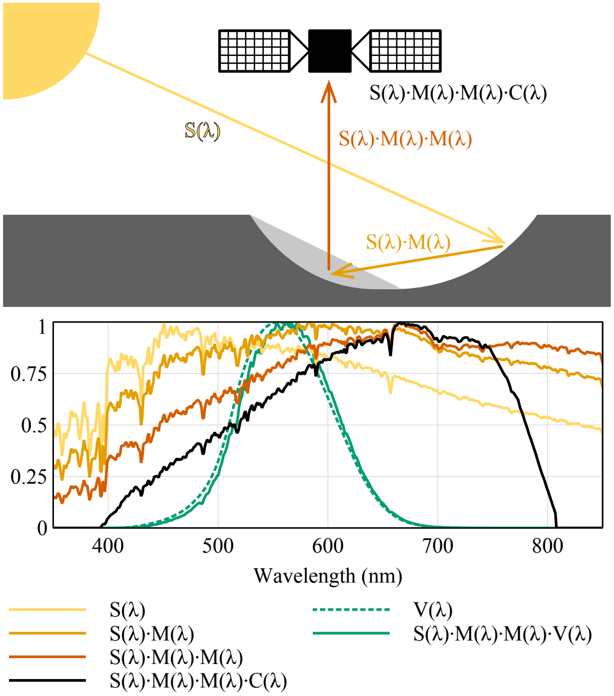

Fig. 4. Path of light illuminating lunar shadows. (a) Diagram of the light path. Solar spectrum $S(\lambda)$ is reflected off of an illuminated lunar surface [reflectance spectrum $M(\lambda)$] into a shadow, then off the shadowed surface [$M(\lambda)$ again], and finally recorded by ShadowCam [response curve $C(\lambda)$]. (b) Spectrum of the light at each stage, scaled to 0–1, with $V(\lambda)$ and the final spectrum convolved with $V(\lambda)$ included for comparison.

denoted $SMM_{cal}(\lambda)$ in units of W/m^2/sr (see Fig. 4).

$$SMM_{cal}\left(\lambda\right)=S\left(\lambda\right)\times M\left(\lambda\right)\times M\left(\lambda\right)\times X \quad (3)$$

where X is an unknown scaling factor that calibrates the curve to radiance units. To find X, we define an additional curve, $C_{cal}(\lambda)$, that satisfies Eq. (4).

$$\int_{380\text{ nm}}^{830\text{ nm}} true\ spectrum\left(\lambda\right)\times C_{cal}\left(\lambda\right)d\lambda=R \quad (4)$$

where R is the radiance value that the standard ShadowCam calibration pipeline returns for an image of a surface with a given spectrum, and 380–810 nm covers the full range of photon wavelengths ShadowCam can detect.

To find $C_{cal}(\lambda)$, we used ShadowCam laboratory calibration images along with the recorded calibrated spectra of the light entering the camera for each image (Supplementary data; Humm et al. 2023). We calculated $C_{cal}(\lambda)$ by scaling the published ShadowCam spectral response curve to minimize sum-of-squares difference between the median ShadowCam-measured radiance of each image and the result of Eq. (4) for that image for the 26 calibration images where > 75% of the observed energy fell within ShadowCam's nominal response range. We checked this estimate using the Microsoft Excel Solver function to produce a new response spectrum from scratch at 10nm point spacing using all 28 images (constrained to increase from 400–700 nm and decrease from 730–800 nm); the two methods differ by < 5% (mean –0.8%) between 430 and 750 nm.

Given $C_{cal}(\lambda)$, it becomes simple to find X, and thus $SMM_{cal}(\lambda)$, for a radiance of 1 W/m^2/sr/μm: simply insert the definition of $SMM_{cal}(\lambda)$ (Eq. 3) as the true spectrum term in Eq. (4):

$$\int_{380\text{ nm}}^{830\text{ nm}} S\left(\lambda\right)\times M\left(\lambda\right)\times M\left(\lambda\right)\times X\times C_{cal}\left(\lambda\right)d\lambda=R \quad (5)$$

and solve for X with $R = 1$. This properly-scaled $SMM_{cal}(\lambda)$ spectrum can then be used to calculate the luminance of that hypothetical radiance = 1 scene by dividing Eq. (1) by 1 W/m^2/sr/μm:

$$\frac{luminance}{radiance}=\int_{380\text{ nm}}^{830\text{ nm}} SMM_{cal}\left(\lambda\right)\times V\left(\lambda\right)d\lambda\times 683\frac{\text{lm}}{\text{W}}$$
$$=70\frac{\text{cd/m}^2}{\text{W/m}^2\text{/sr/}\mu\text{m}} \quad (6)$$

Thus, for a ShadowCam image of shadowed lunar highlands terrain, you can multiply the calibrated radiance values by 70 to get calibrated luminance values in cd/m^2.

We did not reproduce this full process to get a conversion factor for the LROC NAC. However, as the ShadowCam and LROC NAC spectral responsivity curves have very similar shapes (Fig. 3), we assume that the conversion factors are similar for identical input spectra. Removing the second lunar bounce from the $SMM_{cal}(\lambda)$ spectrum gives a ShadowCam conversion factor of 76, so we use that value as the LROC NAC conversion factor for sunlit terrain.

2.4.1 Validation

To determine the accuracy of the ShadowCam luminance conversion factor, we calculated hypothetical conversion factors using various permutations of the input spectra. For example, using the Solver-derived ShadowCam response curve instead of the scaled curve from Humm et al. (2023) gives a conversion factor of 71 instead of 70.

If instead of the photopic luminous efficiency curve, we use the scotopic curve (ISO 2023), appropriate for fully dark-adapted eyes in very dark environments (< –4 EV), a luminance lower than ShadowCam can measure, the conversion factor would be 130; the mesopic conversion values for any given value of dark adaptation will lie between that value and 70. Thus, in places where the luminance is below 5 cd/m^2 (~4 EV), if astronauts have fully dark-adapted to that environment (most likely by looking away from the lit crater wall for several minutes), they may perceive the terrain to be brighter by up to a factor of two (+1 EV) than the photopic luminance values given in this paper.

Our use of the Apollo 16 (mature highland material) spectrum for the lunar surface assumes that it is a rough match for the broadly-anorthositic polar regions. This spectrum might not be an optimal match, especially inside permanent shadows, which may differ from the spectra of sunlit surfaces (e.g., Li et al. 2018; Parkinson et al. 2023). Observations from Moon Mineralogy Mapper suggest potential water-ice content up to 30 wt% in a few locations (Li et al. 2018); ShadowCam observations confirm that these locations cannot have >30 wt% water-ice (Ando et al. 2025). Thus, as a test of the effect different lunar spectra have on the conversion factor, we replaced the second-bounce (shadowed surface) lunar spectrum with a spectrum of highland regolith simulant mixed with 30% water ice (Parkinson et al. 2023). This regolith+ice spectrum produced a conversion factor of 74.

We calculated the conversion factor for a perfectly flat incoming spectrum; that is, for a radiance of 1 W/m^2/sr/μm, assuming each 1 nm slice of the spectrum has a radiance of 0.001 W/m^2/sr. This simplification results in a conversion factor of 73, indicating that our nominal conversion factor of 70 is robust.

We consider our radiance-to-luminance conversion factor of 70 (cd/m^2)/(W/m^2/sr/μm) to be accurate to within ± 5%. Note that due to EV being a Log$_2$ scale, an uncertainty of ± 5% in luminance is an additive ± 0.1 EV.

3. RESULTS AND ANALYSIS

3.1 Large Permanently Shadowed Regions

For large PSRs, summer maximum luminance levels range from a low of ~2.5 EV in Amundsen crater to a high of 8 EV in Sylvester N crater (Figs. 5 and 6). Typical variation in maximum luminance is < 3 EV (a factor of 8), although there are outliers with much larger variation (Fig. 5). Peak luminance levels usually last on the order of one week in each lunation (Fig. 6). Radiance variation of square-kilometer patches within a few kilometers of the central measurement point is typically on the order of a factor of 2 (± 0.5 EV). Note that an astronaut standing on the surface would see much higher local variations due to local secondary shadowing and brighter slopes facing towards the source of the secondary illumination.

Maximum summer PSR luminance is correlated with both depth/diameter ratio (d/D) and diameter (Fig. 5(b) and 5(c)); the correlation between diameter and luminance

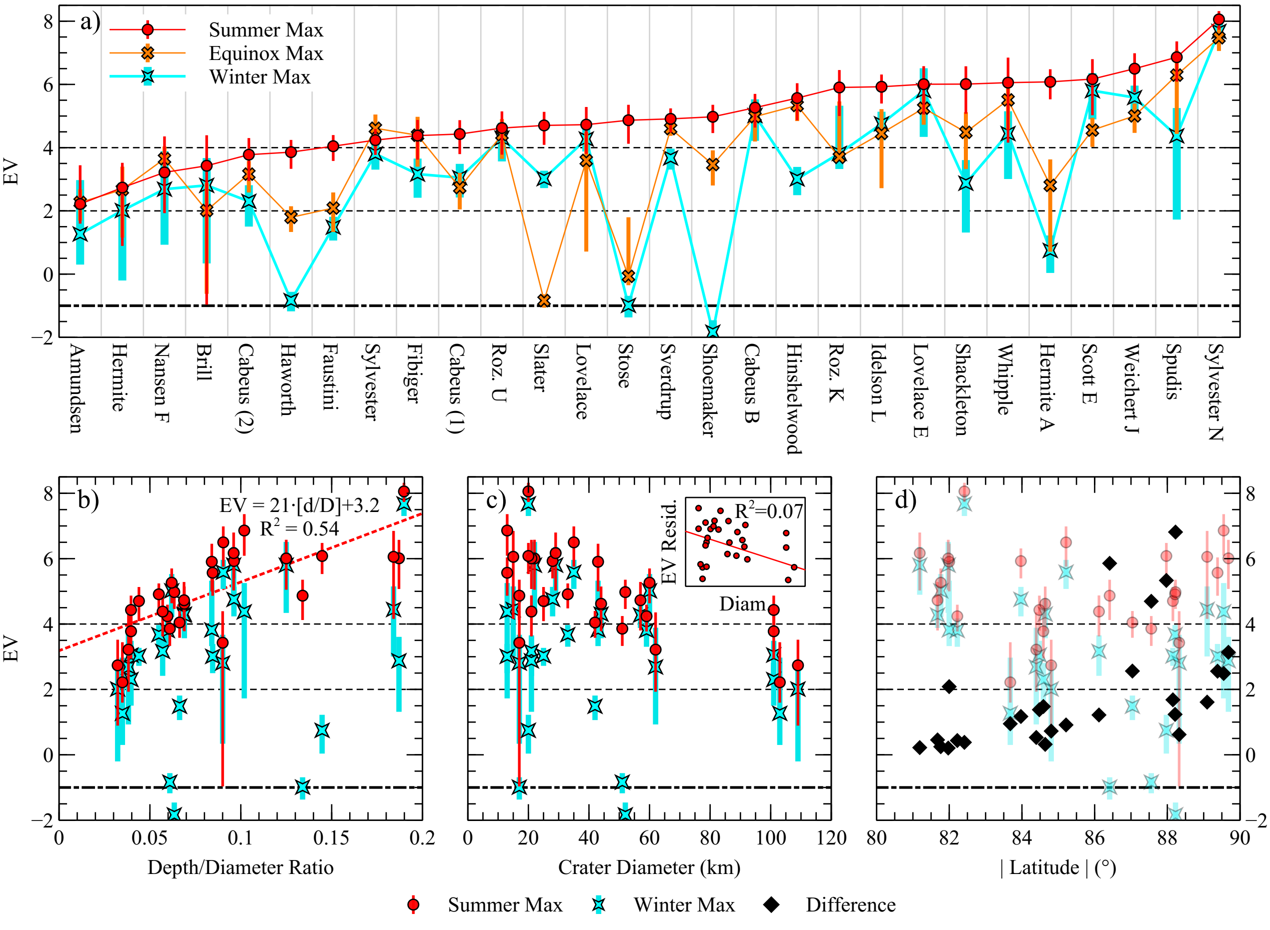

Fig. 5. Luminance results for large PSRs. (a) Variations in maximum observed luminance of target point (see Section 2.1) by crater and season. The two Cabeus sites demonstrate variation within a large PSR (site 1 is near the LCROSS impact site, while site 2 is 12 km east). While the peak luminance of these sites only differs by approximately a factor of two (1 EV), the time-of-day of peak luminance differs by ~144 hr. Error bars show Sd among the 80 surrounding points at that time-of-day. At some point between the horizontal dashed lines at 4 and 2 EV astronauts will likely start needing supplemental light for investigating geologic samples; the line at –1 EV marks the approximate ShadowCam noise floor. (b) Max summer and winter luminance vs. d/D. (c) Max summer and winter luminance vs. diameter. Inset shows correlation of diameter with the residuals of the EV vs. d/D ratio fit from (b). (d) Max summer and winter luminance, and difference between them, vs. degrees of latitude from the equator. d/D, depth/diameter ratio; PSR, permanently shadowed region; EV, exposure value; Roz, Rozhdestvenskiy.

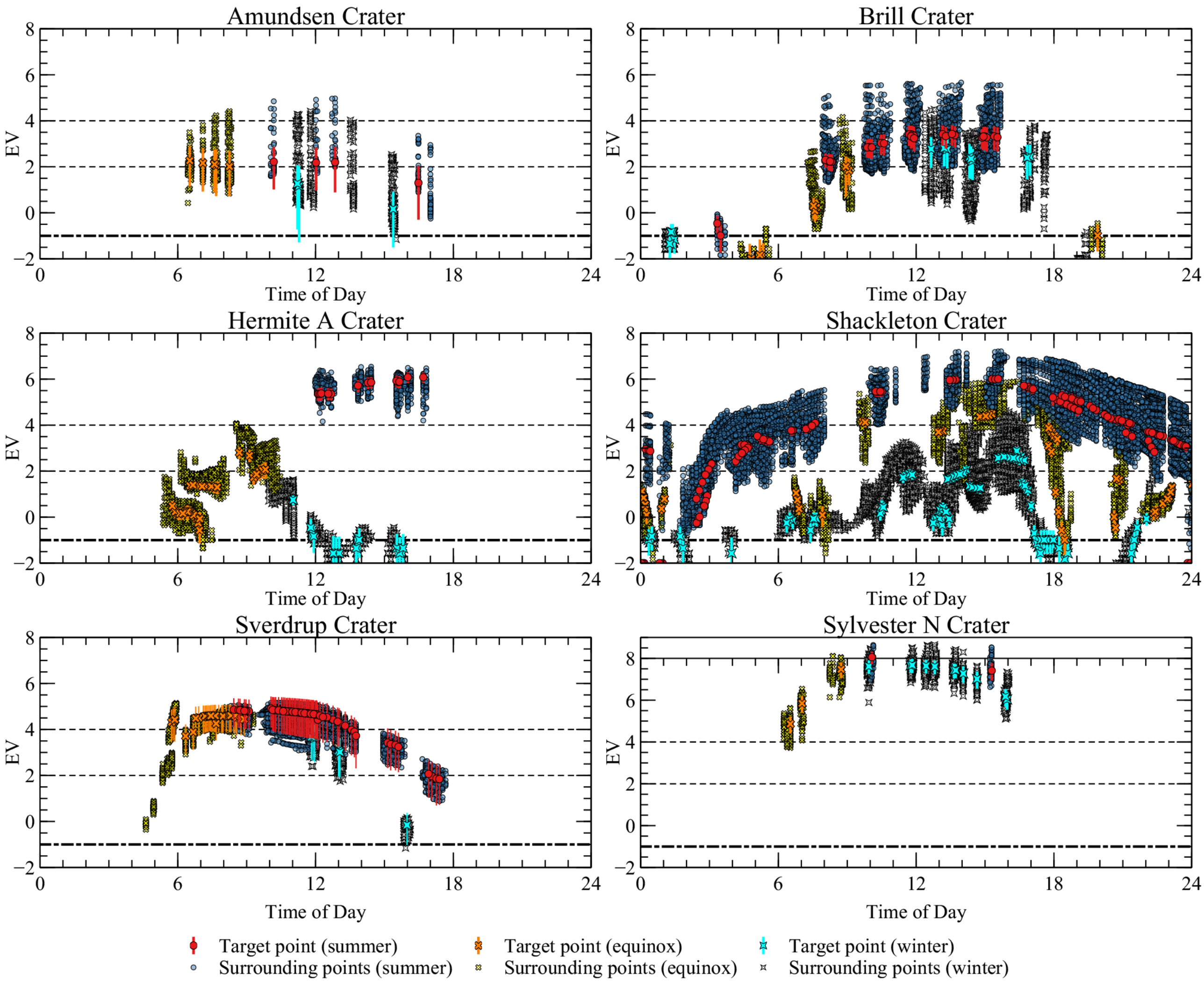

Fig. 6. Sample of EV values for target point and surroundings for large PSRs. Error bars show SD of luminance of 2 m px in the 1.2 km square surrounding the target point. Off-scale low values are marked at –2 EV. EV, exposure value; PSR, permanently shadowed region.

seen in Fig. 5(c) is almost entirely due to a correlation between diameter and d/D ratio among this sample of craters, with little more than a hint of it remaining after subtracting a linear fit to d/D (Fig. 5(c)). These correlations indicate that the primary influence on light within a PSR is the geometry of the crater it lies within: taller and closer sunlit walls reflect more light into the shadow. Latitude has no significant influence on summer luminance. Seasonal variation, however, does correlate with latitude (Fig. 5(d)), craters closer to the pole having greater seasonal differences, as well as a threshold where craters pole-ward of 86° latitude potentially have much larger differences (≥ 4 EV) than the general trend (0–2 EV).

In our dataset, there are several sites where the equinox maximum observed radiance is lower than the winter maximum (e.g., Brill crater; Fig. 5). This observation is likely an artifact of incomplete time-of-day coverage for each season, especially for the equinox periods. The KPLO orbit exhibits rough synchronization between the sub-spacecraft time-of-day and the season; the two parameters both vary on a roughly one-year cycle, with only a few weeks difference in period. Additionally, some sites are imaged more frequently than others depending on their latitude and scientific priorities. It so happens that at many sites, coverage was obtained in summer and winter at times-of-day close to the maximum luminance; however during the equinox period the time-of-day coverage misses the peak (Fig. 6).

3.2 Small Permanently Shadowed Regions

Small PSRs, such as the Artemis astronauts may initially explore, have radiances similar to multi-km scale PSRs (Fig.

7). While our sample size is limited, the seasonal variation we observe is also similar to that for large PSRs: Four of the five PSRs have winter maxima within 2 EV of the summer maxima, while the fifth (Dawa) is almost fully shadowed by the rims of Jaci and Masina in winter and thus has interior luminance below the ShadowCam detection limit (more than 6 EV lower than in summer). We do observe more abrupt changes in illumination in some small PSRs than in large ones, as a result of shadows from distant terrain plunging the entire area into shadow. A dramatic example can be seen in the winter curve for Marston crater in Fig. 7, where luminance drops from near its seasonal maximum to below the ShadowCam detection limit for ~0.5 time-of-day units (~14 Earth hr) before returning to full brightness, as the shadow of a distant feature briefly sweeps across the region.

Our sample of craters, while limited in number, allows a comparison of the effects of morphology independent of regional or latitudinal effects. H crater, Jaci, Masina, and Dawa form a sequence from crisp (H crater) to degraded (Dawa), are all within a 22 km region, and show a gradation of maximum luminance from ~7.5 EV to ~5 EV, correlating with degradation state. This is qualitatively similar to our finding of d/D ration as the primary driver of luminance in large PSRs, although a larger sample size would be beneficial to quantify this pattern and show that it holds for the majority of shadows in small craters.

The time of day that peak luminance occurs depends strongly on local topography. Within the ~5 km wide VIPER region (Fig. 7), Masina crater (on the eastern side of the site) has peak shadow luminance first during each lunation, Dawa crater (in the middle) peaks second, and Jaci crater (the westernmost) peaks third, ~7 Earth days after the Masina shadow reached peak luminance. This variation is likely due to a topographic maximum in the center of the site where their rims intersect. Marston crater is an even more extreme case: although its longitude is ~223°E, so local noon is when the sub-solar point is at 223°E longitude, it is on an Earth-facing slope of a ridge that runs almost directly away from the pole, so its peak luminance instead occurs when the sub-solar point is at ~340° longitude (roughly perpendicular to the ridgeline). Marston is also an example of regional secondary lighting: For almost the entire "night" in summer, although it receives no direct sunlight, the upper portion of its walls and most of its surroundings are still illuminated to a level of ~1–3 EV by secondary light reflecting from some distant surfaces to the east. During this time, the PSR on the floor of Marston crater is in secondary shadow, below the ShadowCam detection limit of approximately –1 EV, and so this regional secondary lighting does not show up in Fig. 7.

3.2.1 Case Study: IM-2 Landing Site

H crater (unofficial name, 200 m diameter) is 900 m north of the IM-2 landing site (84.761°S, 29.165°E). The floor is permanently shadowed and large enough for ShadowCam to image. Additionally, at most times of day, its rim casts a shadow outside of the crater that is a good analogue for the types of large shadowed areas that an astronaut on foot could visit on early Artemis missions (the walls of H crater are likely too steep for astronauts to traverse, and as

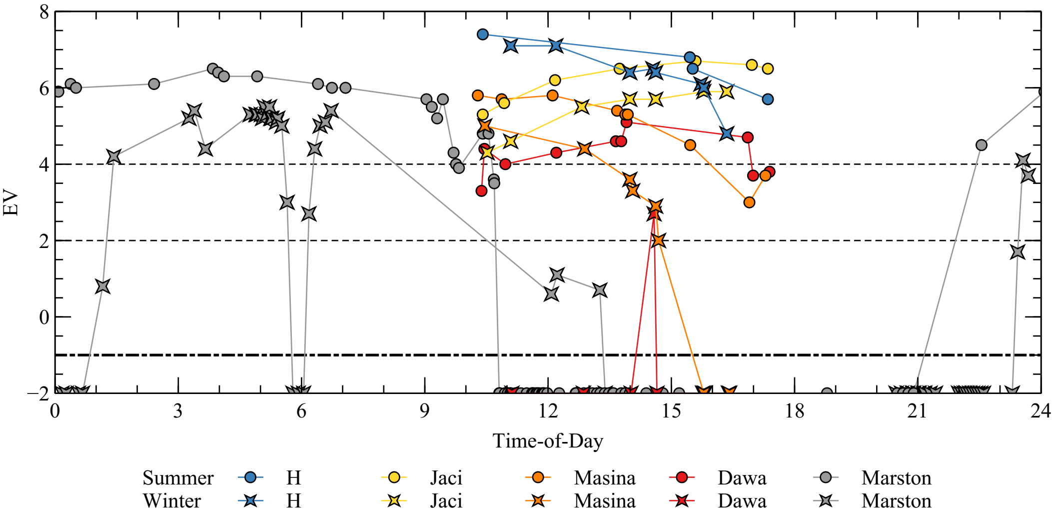

Fig. 7. Small PSR EV values vs. time-of-day. Points marked at –2 EV show no evidence of terrain-related signal in > 50% of the crater interior. EV, exposure value; PSR, permanently shadowed region.

such reflect more light to the floor than in shallower, safer craters).

We evaluated the interior illumination within H crater with pairs of nadir-looking ShadowCam and LROC NAC images acquired with similar lighting (typically sub-solar latitudes within 0.05° and sub-solar longitudes within 2°; see Table 4). The image sets were aligned with a NAC terrain model, using features in temporary shadows to align the ShadowCam images, and the images from both cameras were calibrated to radiance. The ShadowCam images were overlain on shadowed areas of the NAC images (radiance < 1 $W/m^2/sr/\mu m$, approximately 9 EV). This mosaicking produced high-dynamic-range images with high-SNR values over all but a sliver at the boundary of the shadow (Fig. 8). We collected radiance values along profiles defined in orientations relative to the sunlight vector (Fig. 8). Stray light correction per Section 2.2 was done only for ShadowCam values. Note that these seven ShadowCam images were inspected for artifacts that can occur adjacent to saturated terrain, and because none were present, the 18-pixel cropping mentioned in Section 2.2 was omitted. Because the shadowed areas at H crater in all of these images are <200 m in diameter (except for the 90.3° incidence pair), we expect the darkest pixel within H crater to be representative of the stray light value, and subtracted it from the shadowed portions of each profile (see Supplementary Data).

We found that the luminance difference between the shadowed interior of H crater and the flat-lying sunlit surfaces outside was typically 5-7 EV, or a factor of ~32-128 (Table 4). The sunlit interior wall, being more directly oriented towards the Sun, was typically an additional factor of two brighter than the surroundings, for a maximum contrast of ~8 EV (a factor of ~256).

During final approach to the landing site during the IM-2 robotic landing mission, the Athena lander flew near H crater and captured images with its wide-angle cameras at 1.25, 2.5, and 5 ms exposures. These Canadensys "NISA" model cameras use a sensor with a linear response of pixel value (digital number, DN) per unit radiance, which we validated across the full detection range of the camera in laboratory testing for the Grace μNova hopper, so although the specific cameras on Athena were not calibrated to absolute radiance or luminance, we can accurately determine relative radiance levels within an image. An additional complication is that the raw images were not returned due to bandwidth constraints; the available images were compressed with the JPEG algorithm for transmission, and the original 12-bit data compressed to 8 bits using the sRGB transfer (or "gamma") function (Anderson et al. 1996). This is a piecewise function that preferentially preserves radiance level details at the bottom end of the dynamic range. For IM-2 images, it is linear for original 12-bit DN_{12}s < 13 ($DN_8 = DN_{12} \times 0.8075$), and a power law function for DN_{12}s 13 and above ($DN_8 = DN_{12}^{1/2.4} \times 8.44 - 14.08$). The primary impact of JPEG compression at low radiance levels was to average out details smaller than its 8 × 8 px block size.

In the 5 ms image, the crater interior has higher pixel values than pixels observing space, and there is a low-frequency pattern consistent with ShadowCam image M035790655S, which was acquired under similar lighting conditions (Fig. 9). Although there is no fine geomorphic detail visible inside H crater due to the JPEG compression,

Table 4. Luminance inside and outside shadow of 200 m south polar H crater

Image ID[1]	Time-of-day	Sub-solar Lat	Sub-solar Lon	Incidence	Outside EV	Lit wall EV	Inside EV	Outer shadow EV
M111383847L	10.1	1.54°S	57.96°	83.9°	13	14	8	N/A
M018137591S	10.4	1.30°S	52.94°					
M124401181L	12.3	1.51°N	24.94°	86.3°	12–13	14	7	N/A
M031067746S	12.2	1.52°N	26.20°					
M1169489046R	9.3	0.53°N	69.88°	86.6°	12–13	13–14	6–7	N/A
M066469648S	9.3	0.50°N	70.07°					
M1210258443L	8.6	0.67°N	80.47°	87.4°	12	13–14	5–7	4–8
M035790655S	8.7	0.70°N	78.67°	87.3°				
M1231407146L	15.7	1.08°N	333.50°	88.1°	12	13–14	5–6	0–6[2]
M026352517S	15.7	1.04°N	333.30°					
M1371902786R	17.0	1.34°S	313.82°	87.8°	11–12	13–14	4–6	0–6[2]
M072436787S	17.4	1.29°S	308.81°					
M1374613372R	18.5	0.73°S	291.17°	90.0°	2–8[3]	11–12[3]	<–1[3]	0–3[3]
M039396523S	18.6	0.50°S	290.36°	90.3°				

[1] Last character of image name indicates camera: L, LROC NAC Left; R, LROC NAC Right; S, ShadowCam.
[2] Using stray light correction for crater interior, which may be too high for exterior shadow. Actual values may be 1–2 EV higher.
[3] No light reflected from interior crater wall, entire region lit by reflection from some distant landform, except for patches of grazing direct sunlight.
EV, exposure value.

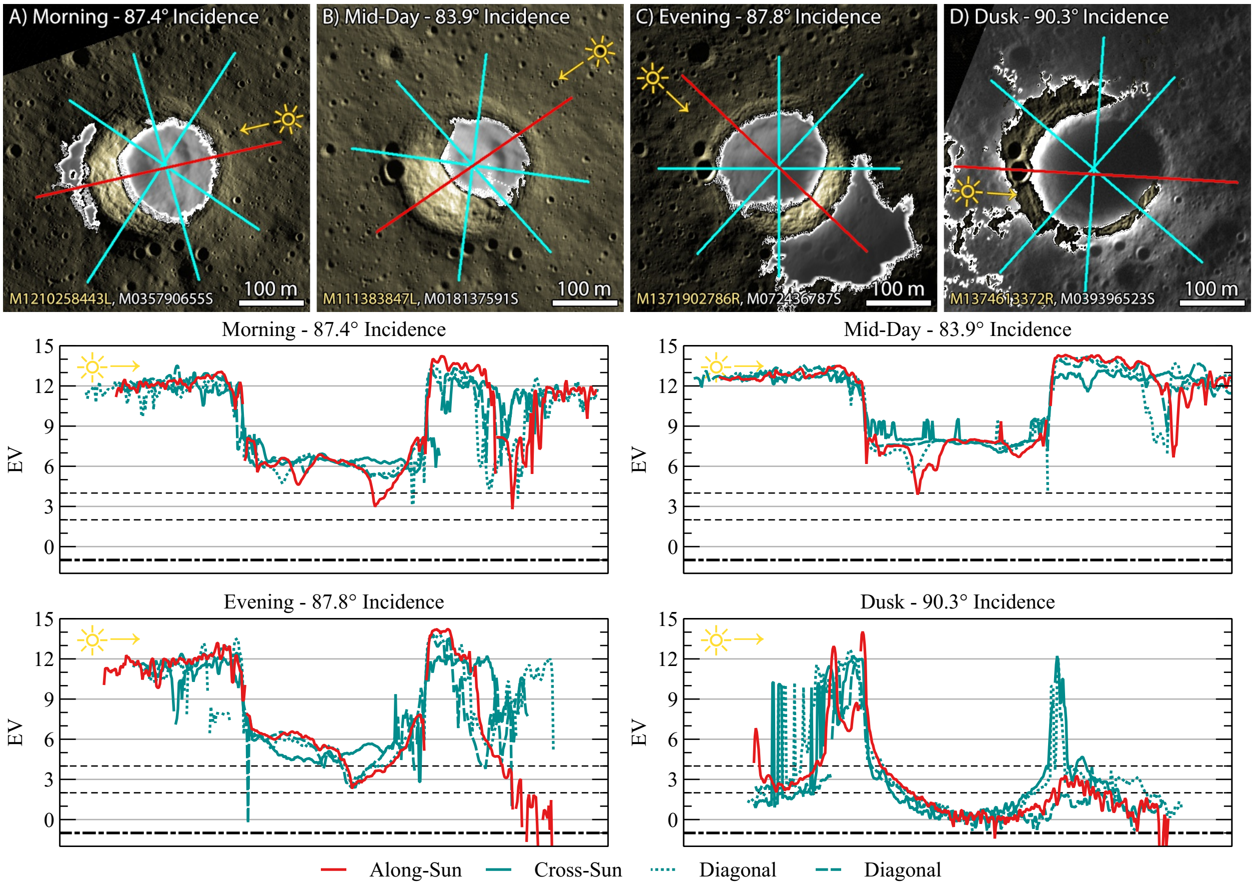

Fig. 8. Luminance profiles across H crater. Top row: Merged LROC NAC/ShadowCam mosaics of H crater (separate stretches inside and outside of the H crater shadow; directly-illuminated ground is artificially tinted yellow). Lines mark profiles shown in the plots below. Bottom plots: Luminance profiles through the H crater shadow. Profiles are scaled horizontally so that the edges of the shadow align in all profiles. For non-cross-sun profiles, sunlight is coming from the left side of plot. LROC NACs, Lunar Reconnaissance Orbiter Narrow Angle Cameras.

we interpret that the overall pixel values within H crater in the IM-2 image are a real signal, and we expect that the pixel values inside and outside the crater in this image should be consistent with Table 2.

Indeed, after correcting the IM-2 images for the sRGB compression, pixel values inside the shadow in H crater range from 11–16, while the mean value for a patch outside the crater is 610, and the lit wall is ~2,350 (the crater wall is saturated in the 5 ms IM-2 image due to color processing quirks; we measured its value from the 2.5 ms image and adjusted for exposure time). These values correspond to the surrounding terrain exhibiting ~50× greater illumination than the crater interior (i.e., 6 EV higher than the shadow) and the wall ~200× brighter (7.5 EV higher than the shadow), in line with the luminance differences from orbital images given in Table 4, particularly for the similarly-lit image pair acquired at time-of-days 8.6 and 8.7.

3.3 Analogue Testing

We verified our luminance and EV conversions with a calibrated spectral light source replicating the expected spectral radiance of PSR surfaces and measured its output with a commercial light meter. Additionally, we evaluated the impact these lighting levels might have on astronauts, by both setting up a workspace with illumination similar to that in PSRs and working at it, and by finding everyday scenes with similarly-luminous surfaces.

3.3.1 Spectral Source

We confirmed the accuracy of our luminance conversion factor by acquiring measurements from a calibrated Gamma Scientific RS-7-6 wide field of view LED-based tunable spectral source set to replicate the radiance levels observed in ShadowCam images. This spectral source was also used to calibrate ShadowCam, although it was modified and

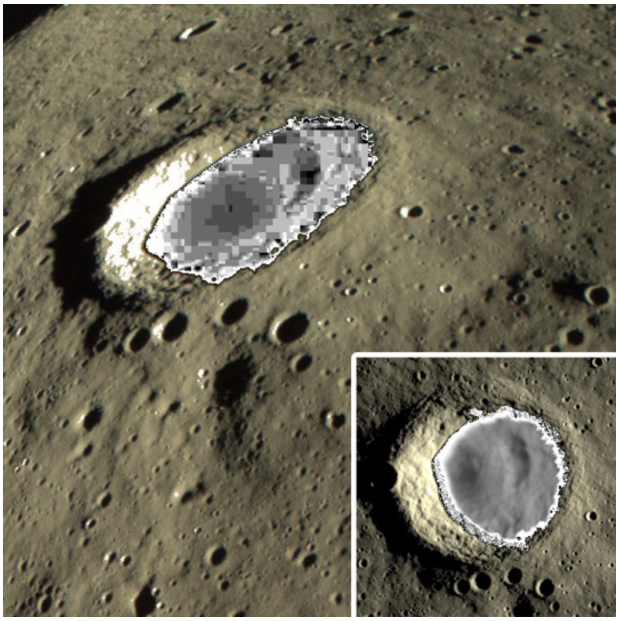

Fig. 9. Oblique view from IM-2 Athena lander looking north at 200 m diameter H crater from ~300 m altitude (image IM2-F-2522-2-DEC, 5 ms exposure time). Separate stretches for interior and exterior of crater, directly-illuminated ground is artificially tinted yellow. Inset: Merged LROC NAC/ShadowCam image acquired with nearly identical lighting, with similar independent stretches and tinting to the IM-2 panel (NAC M1210258443L, ShadowCam M035790655S).

recalibrated by the manufacturer with a different output diffuser system designed for wide angle cameras before the testing described here. The light source was calibrated 21 months before these measurements with a one-year certification, but was only lightly used in that time and, as it uses LEDs rather than limited-lifespan incandescent bulbs, we believe it was still accurate. The light source can reproduce spectra between 380 and 1,000 nm, with a radiance range of ~0.062–62 W/m^2/sr/μm integrated over the ShadowCam 0.40 μm spectral range (400–800 nm; Humm et al. 2023). We tuned the light source to replicate the $SMM(\lambda)$ spectrum (see Section 2.4; spectrum is available in the Supplementary data), and varied the integrated output radiance from 0.1–30 W/m^2/sr/μm. We measured the RS-7-6 luminance with a handheld light meter (Gossen Luna-Pro F) and a cell phone app (Lightme on an iPhone 12 Mini). Additionally, the light source reports its commanded and actual luminance values in cd/m^2. Results are shown in Table 5. The room background light level was below the bottom end of the valid range of the light meter (EV –5, or < 0.004 cd/m^2).

The test results matched our conversions of observed ShadowCam radiance values to luminance and EV to within 2%. The Gossen light meter consistently recorded values 0.2–0.3 EV below our calculated EV based on the reported

Table 5. Light source testing

Reported Radiance1) (W/m^2/sr/μm, 400-800 nm)	Calculated Luminance2) (cd/m^2)	Reported Luminance1) (cd/m^2)	Calculated EV3)	Gossen Light Meter EV4)	Lightme App EV4)
0.000	0.00	0.00	N/A	< –5.00	N/A
0.049	3.45	3.48	4.80	4.50	4.33
0.061	4.29	4.26	5.09	4.75	4.67
0.086	6.02	6.07	5.60	5.33	5.17
0.108	7.56	7.63	5.93	5.67	5.50
0.142	9.96	10.05	6.33	6.00	5.75
0.165	11.55	11.69	6.55	6.33	6.00
0.188	13.16	13.30	6.73	6.50	6.25
0.235	16.45	16.59	7.05	6.75	6.50
0.292	20.46	20.64	7.37	7.00	6.75
0.349	24.40	24.60	7.62	7.33	7.00
0.407	28.49	28.70	7.84	7.67	7.17
0.521	36.45	36.75	8.20	7.83	7.67
0.579	40.51	40.80	8.35	8.17	7.83
1.155	80.85	81.10	9.34	9.00	8.75
2.309	161.6	161.7	10.34	10.17	9.75
4.617	323.2	322.9	11.33	11.17	11.00
9.265	648.6	645.5	12.33	12.17	12.25
18.640	1,305	1,292	13.33	13.00	13.25
28.080	1,966	1,937	13.92	13.67	13.83
32.838	2,299	2,260	14.14	13.83	14.17

1) From the RS-7-6 control software; radiance was reported in μW/cm^2/sr, and multiplied by 40 to convert to W/m^2/sr/μm over the ~0.4μm range used in this test.
2) Using the reported radiance and the conversion factor of 70 from Section 2.4.
3) Using measured luminance and EV conversion formula from Section 1.4.
4) Recorded at the nearest 1/6 or 1/4 EV.
EV, exposure value.

luminance of the light source [this may be due to the use of a different calibration constant; using the lowest value permitted by ISO (1994), 10.6, would make our calculated EVs match the Gossen recorded values]. The phone app was consistently a further ~0.25 EV below the Gossen in the range of EVs found in PSRs.

3.3.2 Permanently Shadowed Region Analogue Scenes

To experience low PSR illumination levels (EV 3–5), we simulated them as part of testing the camera and lighting system for the Grace μNova hopper experiment on the IM-2 mission (Martin et al. 2025). We covered a table with paper printed with ~85% saturation black (to approximate the mean highland regolith albedo), adjusted the lighting in the room to give light meter readings from the paper of EV 3, 4, and 5, and worked at the table while testing the camera (Fig. 10(a)). EV 5 felt like normal room lighting; EV 3 felt distinctly dim, but did not impede working with small objects or reading ~8–10 point text at normal speed. Similarly, the preferred office lighting for many of the people in our research group is darker than many PSRs (Fig. 11).

Additionally, we found that outdoor scenes shortly after sunset contain many surfaces in the luminance ranges found in PSRs (Fig. 10(b)). However, we note that since many of the materials in Fig. 10(b) are more reflective than lunar regolith, the total incoming light in this scene is likely lower than for a similarly-luminous lunar shadow.

4. DISCUSSION

Within large PSRs, we expect astronauts and uncrewed vehicles to have no difficulty operating during the time period each when lighting is optimal each month (approximately one week duration), regardless of season, except in winter in the subset of high latitude PSRs that have high seasonal variation. Luminance levels will be similar to common indoor lighting levels, and while the sunlit terrain casting light into the shadow will be much brighter (comparable to an uncovered window looking out onto a bright sunny day), it will have much less of an impact on visibility than having the Sun low on the horizon outside of shadows. Based on our analogue testing, even the largest and darkest PSRs in summer will be sufficiently illuminated that a human will perceive them as being distinctly dim, but not dark enough to cause impairment: the low end of PSR summer luminance overlaps with recommended lighting for roadways at intersections with pedestrians (Alferdinck 2006). An additional advantage of operating in large shadows over operating in sunlight will be that the diffuse nature of the lighting will prevent the zero-phase shadow-hiding effect that prevented the Apollo astronauts from seeing detail when looking directly away from the Sun.

Small PSRs are more complicated, due to the likely proximity of large expanses of sunlit terrain. In the worst case, the astronaut will be standing in a shadow, but their upper body will still be in sunlight. The specific case of working in a shadow cast by the landing module while having one's helmet in direct sunlight was called out as

Fig. 10. Earth analogues for PSR lighting. (a) Lab setup for testing the imaging system for Grace at potential PSR luminance levels. Light aimed at ceiling in an otherwise-unlit room was adjusted until center of table was at the target EV. (b) Outdoor twilight scene (looking northeast with a building immediately to the west, clear sky, 12 minutes after sunset); reflected luminance was measured at marked locations. Image exposure was adjusted at time of acquisition until the preview qualitatively matched the perceived appearance of the scene. Note that all of these surfaces are more reflective than mature regolith, so there would likely be more ambient light in a crater that has the same luminance as this scene. PSR, permanently shadowed region; EV, exposure value.

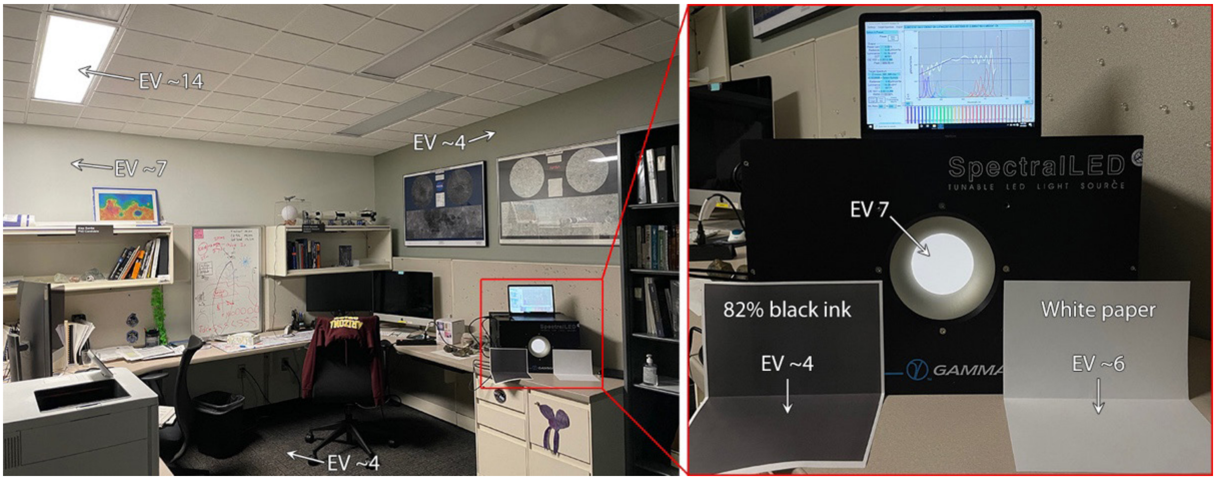

Fig. 11. Example of a spectral light source replicating the SMM(λ) spectrum (Section 2.4) at 7 EV in an office lit by a single fluorescent light. Note that the interior of the spectral source is shaded from the overhead light. The 82% black sheet in front of the spectral source is an approximation of the reflectance of lunar regolith. This lighting was comfortable to work in, and is darker than the peak luminance in the majority of large PSRs in this study. PSRs, permanently shadowed regions; EV, exposure value.

a problem by astronauts on Apollos 11 and 12 due to sunlight shining in their eyes or reflecting within the visor system; they recommended mitigating the problem with adjustable visor systems and minimization of times entering and exiting that shadow (NASA 1969b, d). However, in an experiment by Al Bean on Apollo 12 where he stood in sunlight and observed a contrast chart placed inside a shadow in a crater, with a solar incidence angle of 84° (similar to polar conditions), he was able to discriminate all shades on the chart by holding up a hand to block the Sun and letting his eyes adjust for a few seconds (NASA 1969c, d). For sampling from shallow craters, including craters where the astronauts must enter a "waist-deep" shadow that covers the ground but leaves their heads in sunlight, we recommend that they approach the site from the direction of the Sun, and that the timeline include up to a minute to adjust visor positions and allow for minor dark-adaptation. It may also be beneficial for a companion to stand in sunlight near the sample site to reflect additional light in from their suit onto the scene, although this needs to be balanced against the extra glare the sampling astronaut will perceive from that lit suit.

Craters deep enough that the astronaut is entirely in shadow (Fig. 12) will be easier to work in, but there will still be a period where the astronaut is traversing shadowed terrain while their head is in sunlight. We suggest that astronauts approach large shadows by walking down-Sun, so that their eyes can dark-adapt on the approach, and that extra time be included in the schedule to adjust visors as needed. Once within the shadow with Sun visors raised, however, we do not anticipate any further difficulties, even in the case of a shadow produced by a tall object (such as boulders or the landing vehicle) instead of a crater:

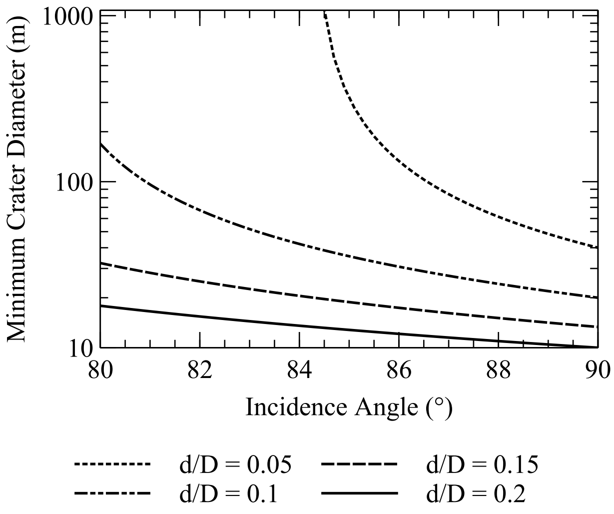

Fig. 12. Minimum crater diameter with ≥ 2 m of shadow depth (astronaut height) at the crater center for different depth/diameter ratios.

> "Okay. It's quite dark here in the shadow and a little hard for me to see that I have good footing. I'll work my way over into the sunlight here without looking directly into the Sun." – Neil Armstrong, Apollo 11 (NASA 1969a).
>
> "Looking up at the LM, I'm standing directly in the shadow now looking up at Buzz in the window. And I can see everything quite clearly. The light is sufficiently

bright, backlighted into the front of the LM, that everything is very clearly visible." – Neil Armstrong, Apollo 11 (NASA 1969a).

"Can't say too much for the visibility right here [in the LM shadow] without the visor up." – Buzz Aldrin, Apollo 11 (NASA 1969a).

"In the shadow, it was very dark. We could see into the shadows, but it was difficult." – Neil Armstrong, Apollo 11 Technical Debriefing (NASA 1969b).

"In the first part of the shadow, when you first move from the sunlight into the shadow, when the Sun is still shining on the helmet as you traverse cross-Sun, you've got this reflection in your face. At this point, it's just about impossible to see anything in the shadow. As soon as you get your helmet into the shadow, you can begin to perceive things and to go through a dark-adaptation process. Continually moving back and forth from sunlight into shadow should be avoided, because it's going to cost you some time in perception ability." – Buzz Aldrin, Apollo 11 Technical Debriefing (NASA 1969b).

"I think we need to modify the visor so that you have a center-top shield that you can pull down and blink the Sun out. If you have that, you can turn 360 degrees and see perfectly in any direction. It will also allow you to look in shadows. The only other time [than when you are looking directly up-Sun that] you have difficulty seeing in a shadow is when some other object is reflecting sunlight into your visor when you're trying to look in the shadow. Once you're in the shadow, you can see well." – Pete Conrad, Apollo 12 Technical Debriefing (NASA 1969d).

"Okay, Houston, I'm looking at the contrast chart in the shadow and, as I mentioned, at 3 feet I can see all six. If I back up maybe to 10 feet, as long as I stand here a moment and adapt my eyes, I can see all six, also. Now, the thing that seems to have the biggest effect on it is how low the Sun is. The Sun is high now and so I don't have to squint my eyes particularly looking in that direction [of the Sun]. Yesterday, looking into the same crater -even though it wouldn't be any darker in there - because the Sun was there, I would never be able to adapt." – Al Bean, Apollo 12 (NASA 1969c).

"The only thing that keeps you from looking into the shadows is if the Sun is low enough so that you can't get your hand up and shield your eyes from the direct ray of the Sun. If you can do that, you can see down in the shadows just like you can on Earth. I was able to do this in this case [looking at a color chart in a shadow in a crater at a solar incidence angle of 84°] and so I could see the full range of blacks in the shadow." – Al Bean, Apollo 12 Technical Debriefing (NASA 1969d).

"I can't see a lot of difference in visibility here as on Earth, really. You adapt just as well… But looking into shadows or anything else like that, it's pretty much the same as on Earth." – Al Bean, Apollo 12 (NASA 1969c).

[When preparing to collect a sample from "about a meter" in the shadow under Shadow Rock:] "I have to get my [gold Sun-protection] visor up to see something." [Later, after Mission Control requested a second sample from underneath the first:] "Let me tip my visor down. That thing is bright. Get out of the Sun. Yeah, I can get that for you." – Charlie Duke, Apollo 16 (NASA 1972a).

"That's a pretty good little skim there. What setting should I open this up to show you these [sampler] prints we got in the [shadow of this ~0.3 m rock] here?" – John Young, Apollo 16 (NASA 1972a).

"When I first got out during the beginning of the EVA I wanted my [gold sun-protection] visor down even in the shade. But after we'd been out in the sunlight during the whole EVA and came back into the shadow, on the closeout, I wanted my visor up because I didn't feel like I could see well enough." – Charlie Duke, Apollo 16 Technical Debriefing (NASA 1972b).

"I have said for 55 years that seeing in the low latitude shadows was no problem due to zero phase 'reflection' and, even though the zero phase point is farther away, I suspect that it will be no problem at the poles. Suit reflection works also." – Jack Schmitt, Apollo 17 (H. Schmitt, personal communication, 29 June 2025).

An uncrewed traverse through a large shadow might sometimes benefit from supplemental near-field lighting for hazard detection, depending on the sensitivity of the camera systems, though trade studies should be made comparing the cost and power draw of sufficiently bright lights to be significant against the costs of designing a camera/vision system that does not need supplemental light (larger detector pixels, lower losses in the optics, using higher analog/digital gain and accepting higher noise in the vision algorithms, etc.), or of pausing/slowing the vehicle to acquire longer exposure images without blurring.

A spacesuit visor system that can block direct sunlight near the horizon at the poles can also block sunlit terrain on the horizon. We recommend that any light-attenuating visor, such as the gold visor on Apollo suits (Lutz et al. 1975), should be adjustable to any height. This feature would allow the visor to darken the horizon without affecting the near field.

Because secondary lighting can change dramatically over the course of a lunation and may be optimal at a time other than local noon, mission planners will need to analyze the local conditions to determine the optimal times for surface activities within each shadow that astronauts are expected to visit. As a practical matter, ShadowCam images will generally not show fine detail within shadows smaller than ~50 m, but at least for minimally-degraded craters such as H crater, we found that the luminance inside the crater can be as dark as ~1/250th of the luminance of the lit wall as measured in LROC NAC images (~8 EV lower; see Section 3.2.1).

Finally, note that we converted radiance values to luminance, that is, the amount of light reflecting off of the surface. Due to the low albedo of the Moon compared to many typical indoor materials on Earth (for example, in Fig. 11, the dark carpet is similar in reflectance to lunar regolith), the illuminance in lunar shadows may be higher than one would expect based on experience in the kinds of scenes described in Table 1. Surface luminance is still a fully appropriate measure for what level of detail astronauts will perceive while driving and inspecting rocks, and whether artificial light is needed for those tasks, but tasks like reading text on paper may be easier than in a room with similarly-bright surfaces by a factor of ~2–4 (see Fig. 11).

5. SUMMARY

The term “permanent shadow” can be misleading, creating a false impression of darkness so complete that a human would see nothing. However, these regions often receive illumination comparable to ordinary indoor lighting. The main factor determining luminance in PSRs is the time of day, while morphology of the host crater—specifically, whether a crater is fresher and sharper or older and more subdued—is the most important factor in the maximum luminance: subdued craters have luminances that are approximately 16–32 times lower than those in fresh craters. Seasonal changes generally alter luminance by less than a factor of four, except in select craters above 86° latitude, where entire regions may remain shadowed for much of the winter.

For large PSRs (> 8 km), we found maximum summer luminances ranging from 2 EV (comparable to twilight scenes on Earth) to 8 EV (comparable to brightly-lit office spaces), with 20 of the 27 PSRs we investigated peaking between 4 EV and 7 EV (see Section 3.1 for details, and Table 1 for EV examples). The period of high luminance during each lunation typically lasts for approximately one week before luminance levels drop more than 1 EV from the peak value. Small PSRs (< 0.5 km) showed comparable patterns: the five we investigated had peak summer luminances ranging from 5 to 7.5 EV, with similar durations of high luminance (see Section 3.2).

Luminance levels and their timing can vary significantly, even between nearby, similarly sized craters. Therefore, excursions within a PSR should be planned after carefully evaluating local lighting conditions. ShadowCam observations are invaluable for traverse planning, especially within 4° of each pole, where repeat coverage is frequent. Except for the ~200 px adjacent to illuminated terrain, ShadowCam images exhibit only minimal stray light, enabling true illumination levels to be accurately quantified. Even within areas with significant stray light, true luminance can still be estimated, and surface features are readily identifiable.

How does high scene contrast affect astronaut comfort and operational efficiency? Sunlit crater walls may be up to 1,000 times brighter than shadowed craters. Apollo astronauts handled similar contrasts by adjusting their visors to block out the sunlit terrain and pausing on entering shadows to raise their Sun visors and let their eyes adjust; similar tactics should work at the lunar poles. Future work could focus on this question by comparing the appearance of hazards such as human-foot-sized rocks within shadows to the detection capabilities of the fully sunlight-adapted human vision system.

5.1 Data Availability

All ShadowCam images used for this work either are available on the PDS at https://data.im-ldi.com/, or will be released by 1 June 2026 for images currently under validation. All LROC NAC images used are available on the PDS at https://data.im-ldi.com/ or https://doi.org/10.17189/1520250. IM-2 descent images are proprietary to Intuitive Machines and currently not available publicly. Key software packages used were the U.S. Geologic Survey Integrated Software for Imagers and Spectrometers (Laura et al. 2022) with modifications by the ShadowCam team, WebPlotDigitizer (Rohatgi 2024), Veusz (Sanders et al.

2023), and custom scripts available in the Supplementary data. Source datasets for all analyses and graphs are also available in the Supplementary data).

ACKNOWLEDGMENTS

We thank the Korea Aerospace Research Institute's Korea Pathfinder Lunar Orbiter teams who developed and operate the Danuri orbiter for providing a platform for ShadowCam and supporting its operations above and beyond the original plan. Their efforts enabled us to collect this robust dataset. We also thank the ShadowCam team for creating and running the instrument, and Intuitive Machines for access to data from the IM-2 mission. We thank Rick Hoppe for assistance with figure production and Zachary Davis for proofreading. Solar spectrum data is courtesy of U.S. Department of Energy/National Renewable Energy Laboratory/Alliance for Sustainable Energy, LLC. This work was funded under the ShadowCam investigation, National Aeronautics and Space Administration contract NNH17CG00C.

ORCIDs

Robert Vernon Wagner
https://orcid.org/0000-0001-5999-0721
Mark Southwick Robinson
https://orcid.org/0000-0001-9964-2932

SUPPLEMENTARY MATERIALS

Supplementary materials are only available online from: https://doi.org/10.5140/JASS.2025.42.4.97

REFERENCES

Alferdinck JWAM, Target detection and driving behaviour measurements in a driving simulator at mesopic light levels, Ophthalmic Physiol. Opt. 26, 264-280 (2006). https://doi.org/10.1111/j.1475-1313.2006.00324.X

American National Standards Institute (ANSI). American National Standard Photographic Exposure Guide: Photographic Exposure Guide ANSI PH2.7-1973 (ANSI, New York, 1973).

American National Standards Institute (ANSI). American National Standard Practice for Office Lighting: ANSI/IESNA RP-1-1993 (IESNA, New York, 1993).

Anderson M, Motta R, Chandrasekar S, Stokes M. (1996). Proposal for a standard default color space for the internet—sRGB. Color Imaging Conf. 4, 238-245. https://doi.org/10.2352/cic.1996.4.1.art00061

Ando J, Li S, Robinson M, Wagner R, Radiance contrasts at possible lunar water ice exposures seen by ShadowCam, Planet. Sci. J. 6, 62 (2025). https://doi.org/10.3847/PSJ/adb8d1

Arnold JR, Ice in the lunar polar regions, J. Geophys. Res. Solid Earth. 84, 5659-5668 (1979). https://doi.org/10.1029/JB084iB10p05659

ASTM International, Standard Solar Constant and Zero Air Mass Solar Spectral Irradiance Tables. ASTM E-490-00a (2019) [Internet], available from: https://doi.org/10.1520/e0490-00ar19

Beyer RA, Shirley M, Colaprete A, Fassett CI, Fernando B, et al., VIPER site analysis. Planet. Sci. J. 6, 236 (2025). Https://doi.org/10.3847/psj/ae061a

Brown HM, Boyd AK, Denevi BW, Henriksen MR, Manheim MR, et al., Resource potential of lunar permanently shadowed regions, Icarus. 377, 114874 (2022). https://doi.org/10.1016/j.icarus.2021.114874

Djachkova MV, Mitrofanov IG, Sanin AB, Litvak ML, Tret'yakov VI, Selecting a landing site for the Luna 27 Spacecraft, Sol. Syst. Res. 56, 145-154 (2022). https://doi.org/10.1134/s0038094622030029

Hapke B, Bidirectional reflectance spectroscopy: 1. theory, J. Geophys. Res. Solid Earth. 86, 3039-3054 (1981). https://doi.org/10.1029/JB086iB04p03039

Hayne PO, Aharonson O, Schörghofer N, Micro cold traps on the Moon, Nat. Astron. 5, 169-175 (2021). https://doi.org/10.1038/s41550-020-1198-9

Humm DC, Kinczyk MJ, Brylow SM, Wagner RV, Speyerer EJ, et al., Calibration of ShadowCam, J. Astron. Space Sci. 40, 173-197 (2023). https://doi.org/10.5140/JASS.2023.40.4.173

Humm DC, Tschimmel M, Brylow SM, Mahanti P, Tran TN, et al., Flight calibration of the LROC narrow angle camera, Space Sci. Rev. 200, 431-473 (2015). https://doi.org/10.1007/s11214-015-0201-8

International Organization for Standardization (ISO), General Purpose Photographic Exposure Meters (Photoelectric Type): Guide to Product Specification (ANSI/ISO 2720:1974 (R1994), 1994.

International Organization for Standardization (ISO), Photometry: the CIE system of physical photometry, ISO/CIE 23539:2023 (2023) [Internet], available from: https://doi.org/10.25039/is0.cie.23539.2023

Jia Y, Zhang Z, Qin L, Ma T, Lv B, et al., Research of lunar water-ice and exploration for China's future lunar water-ice exploration. Space: Sci. Technol. 3, 0026 (2023). https://doi.org/10.34133/space.0026

Kunkel T, Reinhard E, A reassessment of the simultaneous dynamic range of the human visual system, in APGV '10: Proceedings of the 7th Symposium on Applied Perception in Graphics and Visualization, Los Angeles, CA, 23-24 Jul 2010.

Laura J, Acosta A, Addair T, Adoram-Kershner L, Alexander J, et al., Integrated software for imagers and spectrometers (Version 7.1.0) [Computer software] (2022) [Internet], available from: https://doi.org/10.5281/ZENODO.7106128

Lawrence DJ, A tale of two poles: toward understanding the presence, distribution, and origin of volatiles at the polar regions of the Moon and Mercury, J. Geophys. Res. Planets. 122, 21-52 (2016). https://doi.org/10.1002/2016JE005167

Li S, Lucey PG, Milliken RE, Hayne PO, Fisher E, Williams JP, et al., Direct evidence of surface exposed water ice in the lunar polar regions, Proc. Natl. Acad. Sci. 115, 8907-8912 (2018). https://doi.org/10.1073/pnas.1802345115

Litaker HL, Beaton KH, Bekdash OS, Crues EZ, Paddock EJ, et al., South pole lunar lighting studies for driving exploration on the lunar surface, in 46th International IEEE Aerospace Conference, Big Sky, MT, 1-8 Mar 2025.

Lutz CC, Stutesman HL, Carson MA, McBarron II JW, Apollo Experience Report: Development of the Extravehicular Mobility Unit, Technical Report, NASA Technical Note D-8093 (1975).

Mahanti P, Humm DC, Robinson MS, Boyd AK, Stelling R, et al., Inflight calibration of the lunar reconnaissance orbiter camera wide angle camera, Space Sci. Rev. 200, 393-430 (2016). https://doi.org/10.1007/s11214-015-0197-0

Mahanti P, Robinson MS, Humm DC, Wagner RV, Estes NM, et al., Preliminary characterization of secondary illumination at Shackleton crater permanently shadowed region from ShadowCam observations and modeling, J. Astron. Space Sci. 40, 131-148 (2023). https://doi.org/10.5140/JASS.2023.40.4.131

Mahanti P, Thompson TJ, Robinson MS, Humm DC, View factor-based computation of secondary illumination within lunar permanently shadowed regions, IEEE Geosci. Remote Sens. Lett. 19, 8027004 (2022). https://doi.org/10.1109/LGRS.2022.3166809

Mahanti P, Williams JP, Humm D, Lucey P, Robinson, M, et al., Light cues to subpixel temperature characterization in the permanently shadowed regions, in 45th COSPAR Scientific Assembly, Bexco, Busan, Korea, 13-21 Jul 2024.

Martin TD, Agrawal N, Atwell MJ, Bussey DBJ, Estes NM, et al., μNova hopper: *in-situ* exploration of challenging terrains, Proceedings of the 56th Lunar and Planetary Science Conference, The Woodlands, TX, 10-14 Mar 2025.

Mazarico E, Neumann GA, Smith DE, Zuber MT, Torrence MH, Illumination conditions of the lunar polar regions using LOLA topography, Icarus. 211, 1066-1081 (2011). https://doi.org/10.1016/j.icarus.2010.10.030

Narendranath S, Ganesh S, Sahu D, Mishra RK, Bhatt M, et al., Solar system research prospects for the decade and beyond. J. Astrophys. Astron. 46, 34 (2025). https://doi.org/10.1007/s12036-025-10060-0

NASA, Apollo 11 technical air-to-ground voice transcription (GOSS Net 1) (1969a) [Internet], available from: https://ntrs.nasa.gov/citations/20160014392; https://historycollection.jsc.nasa.gov/JSCHistoryPortal/history/mission_trans/AS11_TEC.PDF

NASA, Apollo 11 technical crew debriefing (1969b) [Internet], available from: https://www.nasa.gov/history/alsj/a11/a11tecdbrf.html

NASA, Apollo 12 technical air-to-ground voice transcription (1969c) [Internet], available from: https://historycollection.jsc.nasa.gov/JSCHistoryPortal/history/mission_trans/AS12_TEC.PDF

NASA, Apollo 12 technical crew debriefing (1969d) [Internet], available from: https://www.nasa.gov/history/alsj/a12/a12tecdbrf.html

NASA, Apollo 14 final lunar surface procedures (1971a) [Internet], available from: https://www.nasa.gov/history/alsj/a14/a14lsp.html

NASA, Apollo 14 lunar photography, part I: data user's note (1971b) [Internet], available from: https://ntrs.nasa.gov/citations/19720010767, https://www.nasa.gov/wp-content/uploads/static/history/alsj/a14/A14PhotoIndexPt1.pdf

NASA, Apollo 14 technical crew debriefing (1971c) [Internet], available from: https://www.nasa.gov/history/alsj/a14/a14tecdbrf.html

NASA, Apollo 16 technical air-to-ground voice transcription. MSC-06802 (1972a) [Internet], available from: https://historycollection.jsc.nasa.gov/JSCHistoryPortal/history/mission_trans/AS16_TEC.PDF

NASA, Apollo 16 technical crew debriefing. MSC-06805 (1972b) [Internet], available from: https://www.nasa.gov/history/alsj/a16/a16tecdbrf.html

Null CH, Kaiser MK, Wolters TE, Marquez JJ, Cooter AM, et al., Identification of risks to Eva created by ambient lighting conditions at the lunar South pole, in 12th International Association for the Advancement of Space Safety (IAASS) Conference, Osaka, Japan, 22-25 May 2023.

Ohtake M, Pieters CM, Isaacson P, Besse S, Yokota Y, et al., One Moon, many measurements 3: spectral reflectance, Icarus. 226, 364-374 (2013). https://doi.org/10.1016/j.icarus.2013.05.010

Parkinson AE, Cloutis EA, Applin DM, Turenne NN, Dagdick BR, et al., Detecting and characterizing the abundance and form of water-ice in permanently-shadowed regions of the Moon using a three-band lidar system, Icarus. 400, 115540 (2023).

https://doi.org/10.1016/j.icarus.2023.115540

Robinson MS, Brylow SM, Caplinger MA, Carter LM, Clark MJ, et al., ShadowCam instrument and investigation overview, J. Astron. Space Sci. 40, 149-171 (2023). https://doi.org/10.5140/JASS.2023.40.4.149

Robinson MS, Brylow SM, Tschimmel M, Humm D, Lawrence SJ, et al., Lunar reconnaissance orbiter camera (LROC) instrument overview, Space Sci. Rev. 150, 81-124 (2010). https://doi.org/10.1007/s11214-010-9634-2

Rohatgi A, WebPlotDigitizer [software]. Version 4.7 (2024) [Internet], available from: https://github.com/automeris-io/WebPlotDigitizer/releases/tag/v4.7

Sanders J, Bell G, Graham J, Harris B, Hughes D, et al., Veusz [software]. Version 3.6.2 (2023) [Internet], available from: https://veusz.github.io/

Schonfeld J, Summary of the contracted deliveries of NASA payloads to the Moon via commercial lunar payload services (CLPS), in 2023 IEEE International Conference on Systems, Man, and Cybernetics (SMC), 2024 Honolulu, HI, 1-4 Oct 2023.

Smith M, Craig D, Herrmann N, Mahoney E, Krezel J, et al., The Artemis Program: an overview of NASA's activities to return humans to the Moon, in 2020 IEEE Aerospace Conference, Big Sky, MT, 7-14 Mar 2020.

Wagner RV, Boyd AK, Mahanti P, Robinson MS, Empirical measurements of Earthshine illumination on the Moon, in Presented at the European Lunar Symposium, Padua, Italy, 27-29 Jun 2023.

Watson K, Murray BC, Brown H, The behavior of volatiles on the lunar surface, J. Geophys. Res. 66, 3033-3045 (1961). https://doi.org/10.1029/jz066i009p03033